LANGMUIR

pubs.acs.org/Langmuir Article

Size-Controlled and Sintering-Resistant Sub-3 nm Pt Nanoparticles on Graphene by Temperature-Variation Atomic Layer Deposition

Hao Van Bui,* Sri Sharath Kulkarni, and J. Ruud van Ommen

Cite This: *Langmuir* 2025, 41, 25658−25666 Read Online

ACCESS | Metrics & More | Article Recommendations | Supporting Information

ABSTRACT: Noble metal nanoparticles (NPs), particularly platinum (Pt), are widely used in heterogeneous catalysis due to their exceptional activity. However, controlling their size and preventing sintering during synthesis remains a major challenge, especially when aiming for high dispersion and stability on supports such as graphene. Atomic layer deposition (ALD) has emerged as a promising method to address these issues, yet conventional processes often lead to broad particle size distributions (PSDs). This work introduces a new approach for the deposition of size-controlled and sintering-resistant Pt NPs on graphene by atmospheric-pressure ALD using $MeCpPtMe_3$ and O_2. In this approach, the deposition temperature varies in a cyclic manner in accordance with the Pt precursor and the O_2 exposure steps. In every ALD cycle, the $MeCpPtMe_3$ exposure is carried out at either 150 or 200 °C, and the O_2 exposure is at room temperature. The room-temperature step hinders the diffusion and coalescence of Pt NPs, resulting in significantly narrower PSDs compared to those achieved by the conventional ALD processes at 150 and 200 °C. Importantly, Pt NPs with narrower PSDs exhibit higher catalytic activity and improved stability, which are demonstrated for the propene oxidation reaction, despite having a significantly lower Pt loading. Our approach may open a new avenue toward the size-selection synthesis of noble metal NPs for catalytic applications.

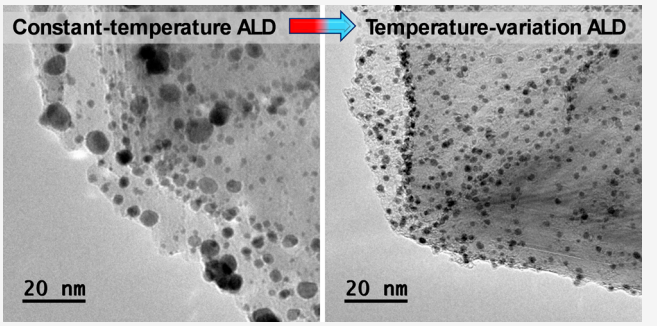

INTRODUCTION

Platinum (Pt)-based catalysts are well-known for their excellent intrinsic catalytic activity and high electron transfer efficiency, particularly in electrochemical reactions such as hydrogen evolution and oxygen reduction.[1,2] Their remarkable resistance to corrosion and oxidation and strong electronic metal−support interactions are additional key factors to ensure high durability and long-term performance in catalytic systems.[3−5] Moreover, the catalytic properties of Pt can be tailored by controlling its size, shape, and surface structure, enabling optimization for specific applications.[6−8] Hence, catalysts based on supported Pt nanoparticles (NPs) are widely used in many chemical reactions and devices, despite the challenges posed by the high cost and limited availability of Pt.[9,10] Addressing these challenges requires synthesis methods that can minimize the Pt loading in the catalysts while maximizing the catalytic performance. With the capability of depositing highly dispersed, uniformly distributed Pt NPs even on high-specific-area substrates[11−16] and the ability to control the particle size precisely at the atomic level,[4,17,18] atomic layer deposition (ALD) has emerged as an effective approach for the synthesis of high-performance Pt-based catalysts.[19−21]

Owing to its advantageous physical and chemical properties, such as high thermal stability, high volatility, high reactivity, and versatility across various substrates, methylcyclopentadienyl(trimethyl)platinum ($MeCpPtMe_3$) is the most established precursor for Pt ALD. $MeCpPtMe_3$ can be combined with an oxidizing agent, such as oxygen (O_2),[22,23] or ozone (O_3),[24,25] or with a reducing agent such as hydrogen (H_2),[26−28] enabling the deposition of Pt in a broad range of temperatures. Among these processes, ALD using $MeCpPtMe_3$ and O_2 is most widely investigated, achieving insights into the surface reaction, nucleation and growth mechanisms of Pt. On the one hand, it has been demonstrated that this ALD process relies on the combustion reactions of the ligands that take place in both half-cycles.[29−33] In the first half-cycle, oxidative reactions occur between $MeCpPtMe_3$ molecules and the chemisorbed oxygen atoms on the surface, which partially consume the ligands of the precursor molecules. The remaining ligands are removed during the O_2 exposure in the second half-cycle, which also restores the chemisorbed oxygen atoms on the surface readily for the reactions with the precursor molecules in the next cycle. On the other hand, the nucleation and growth of Pt on the substrate surface are found

Received: July 10, 2025
Revised: August 24, 2025
Accepted: September 3, 2025
Published: September 9, 2025

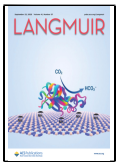

https://doi.org/10.1021/acs.langmuir.5c03532
Langmuir 2025, 41, 25658−25666

to be strongly dependent on the experimental conditions, such as O_2 exposure, O_2 partial pressure and temperature.[23,34,35] Particularly, the O_2 exposure (i.e., the product of partial pressure and pulse time) plays a key role in governing the nucleation behavior of Pt, in which high O_2 exposure not only enables a faster nucleation but also results in a higher Pt loading.[23] The O_2 partial pressure may influence the uniformity of the particle size, in which high O_2 partial pressures result in narrow and symmetric particle size distribution (PSDs), while low pressures result in broad PSDs with a long tails toward the large-size side.[34]

Deposition temperature is one of the most important parameters in ALD. Its influence is commonly reflected by the temperature window, in which the self-saturation of the surface reactions is achieved.[36,37] Particularly for the Pt ALD processes within the temperature window, the deposition temperature additionally affects uniformity of the particle size. Higher deposition temperatures provide higher thermal energies, promoting the diffusion of the deposited Pt across the substrate surface and consequently resulting broad PSDs.[18,23,35,38] In contrast, the Pt NPs deposited at low temperatures exhibit significantly narrower PSDs and higher catalytic performance at the same Pt loading.[39] Notably, Grillo et al. demonstrated that the diffusion of Pt NPs mainly occurred during the second half-reaction, i.e., during the oxygen exposure step.[35] This effect is attributed to the local heat generated by the combustion reactions between the precursor ligands and O_2.[35] This leads to an increase in the local temperature that is considerably higher than the actual deposition temperature, which can unpin and displace Pt NPs, thus promoting sintering via NP diffusion and coalescence.[40]

This work presents a new approach for the deposition of highly uniform and stable Pt NPs on graphene by ALD using $MeCpPtMe_3$ and O_2. We demonstrate that by lowering the temperature during the O_2 exposure step to room temperature, the diffusion and coalescence of Pt NPs are strongly suppressed. This allows for better control of the particle size, resulting in significantly narrower PSDs compared to the conventional ALD. Importantly, despite the oxidation at room temperature, the temperature-variation ALD enables the deposition of highly crystalline and metallic Pt NPs, which are confirmed by high-resolution TEM, XRD and XPS analyses. Furthermore, the Pt/graphene catalyst achieved by the temperature-variation ALD exhibits higher catalytic activity and stability, which are demonstrated by the propene oxidation reactions. Our approach may open a new avenue toward the size-selection synthesis of noble metal NPs for catalytic applications.

EXPERIMENTAL

The ALD experiments were performed using a home-built fluidized bed reactor operating at atmospheric pressure as described elsewhere.[38,41] Briefly, the system consists of a glass column (26 mm in internal diameter and 500 mm in height) placed on top of a single motor Paja PTL 40/40-24 vertical vibration table to assist the fluidization (Figure S1, Supporting Information). ALD of Pt was performed using $MeCpPtMe_3$ (Strem Chemicals, ≥98%) and synthetic air containing 20 wt % O_2. The solid $MeCpPtMe_3$ precursor (initially 10 g) was contained in a stainless-steel bubbler (500 mL) and was sublimed by heating the bubbler to 70 °C. The gas line connecting the bubbler with the reactor was maintained at 80 °C to prevent the condensation of the precursor. Nitrogen (99.999 vol %) was used as the carrier gas. Graphene nanoplatelet powder with a specific surface area of 150 m^2 g^{-1} was obtained from Strem Chemicals. For each experiment, 0.75 g of the powder was used. An optimal N_2 flow of 0.5 L min^{-1} was used to fluidize the powder. Before the Pt deposition, the graphene powder treated in ozone (O_3) at 200 °C for 30 min to generate functional groups on the graphene surface. This was carried out by flowing synthetic air through an OAS Topzone ozone generator, which produced an O_3-enriched air containing about 1.5 wt % O_3.

In the temperature-variation ALD process, each ALD cycle consisted of four steps. In the first step, the temperature inside the reactor was maintained at T_1 (T_1 = 150 or 200 °C) and the precursor vapor was introduced into the reactor for a dosing time of 4 min. In the second step, the reactor was purged by an N_2 flow for 15 min to remove the reaction byproducts and the excess precursor. During this step, the reactor was cooled down to room temperature (i.e., 25 °C). In the third step, synthetic air was introduced for a dosing time of 10 min. In the fourth step, the reactor was purged again by N_2 for 10 min, during which the reactor was heated to the temperature T_1. During this step, any residual O_2 could make a minor contribution to ligand removal if oxidation during the third step was not fully completed.

The morphology of the Pt/graphene was characterized by transmission electron microscopy (TEM). The powder was suspended in ethanol and transferred to regular TEM grids. TEM images were taken using a JEOL JEM1400 transmission electron microscope operating at a voltage of 120 kV. High-resolution TEM images were obtained using a FEI Titan G2 60−300 transmission electron microscope operating at 300 kV. The images were then analyzed by using the ImageJ software to obtain particle size distributions (PSDs). For each PSD, from 3000 to 7000 particles on different TEM images were analyzed.

The crystalline structure of Pt/graphene was investigated by powder X-ray diffraction (XRD) using a PANalytical X-pert Pro diffractometer with Cu Kα radiation (λ = 0.154 nm). The diffractograms were recorded in the 2θ range of 10−90° with fine steps of 0.001°. The elemental composition was characterized by X-ray photoelectron spectroscopy (XPS) using a Thermo Scientific K-Alpha X-ray photoelectron spectrometer (XPS) System (Al Kα radiation with the X-ray photon energy of 1486.7 eV). Survey scans were acquired using a spot size of 400 μm, pass energy 200 eV, and energy step size of 1.0 eV. For the core-level spectrum acquisitions, the spot size, pass energy and step size were 400 μm, 50 eV, and 0.1 eV, respectively. The peaks positions were calibrated according to the C 1s peak at 284.5 eV.

The Pt loadings were determined by instrumental neutron activation analysis (NAA), which was carried out at the Reactor Institute of Delft. The powders (about 30 mg for each Pt/graphene sample) were loaded into high purity polyethylene capsules. The samples and a standard sample (reference) were then packaged and irradiated in a suitable reactor at a constant neutron flux. All reactors used for neutron activation employed uranium fission, which provides a neutron flux in the order of 10^{12} cm^{-2} s^{-1}. These neutrons have low kinetic energy, typically less than 0.5 eV. Upon irradiation, a neutron can be absorbed by the target nucleus (i.e., Pt), forming a radioactive nucleus, which carries its own half-life characteristics. The nuclear decay of the radioactive nuclei produces gamma-rays, which are detected by the NAA detectors, from which the Pt loading was determined. For Pt/graphene samples, the waiting time of 5 days was applied during the decay of radioactive nuclei.

The catalytic performance of the Pt/graphene was evaluated through the oxidation of propene (C_3H_6) using a fixed bed reactor coupled with an analysis unit, as described in the previous studies.[39,42] In brief, the experimental setup consisted of three main sections: feed mixing, reactor, and analysis. In each experiment, the feed mixture was composed of helium (He) carrying 1000 ppm of C_3H_6 and 1 vol % O_2 with a total flow rate of 30 mL min^{-1}. The reactor was a quartz column with a diameter of 4 mm and length of 25 cm, loaded with 15.4 mg of the Pt/graphene catalyst. To prevent the catalyst entrainment, the reactor was first loaded with 50 mg of silicon carbide. The reactor was placed in a furnace, which was capable of withstanding temperatures up to 1000 °C and equipped with a

https://doi.org/10.1021/acs.langmuir.5c03532
Langmuir 2025, 41, 25658−25666

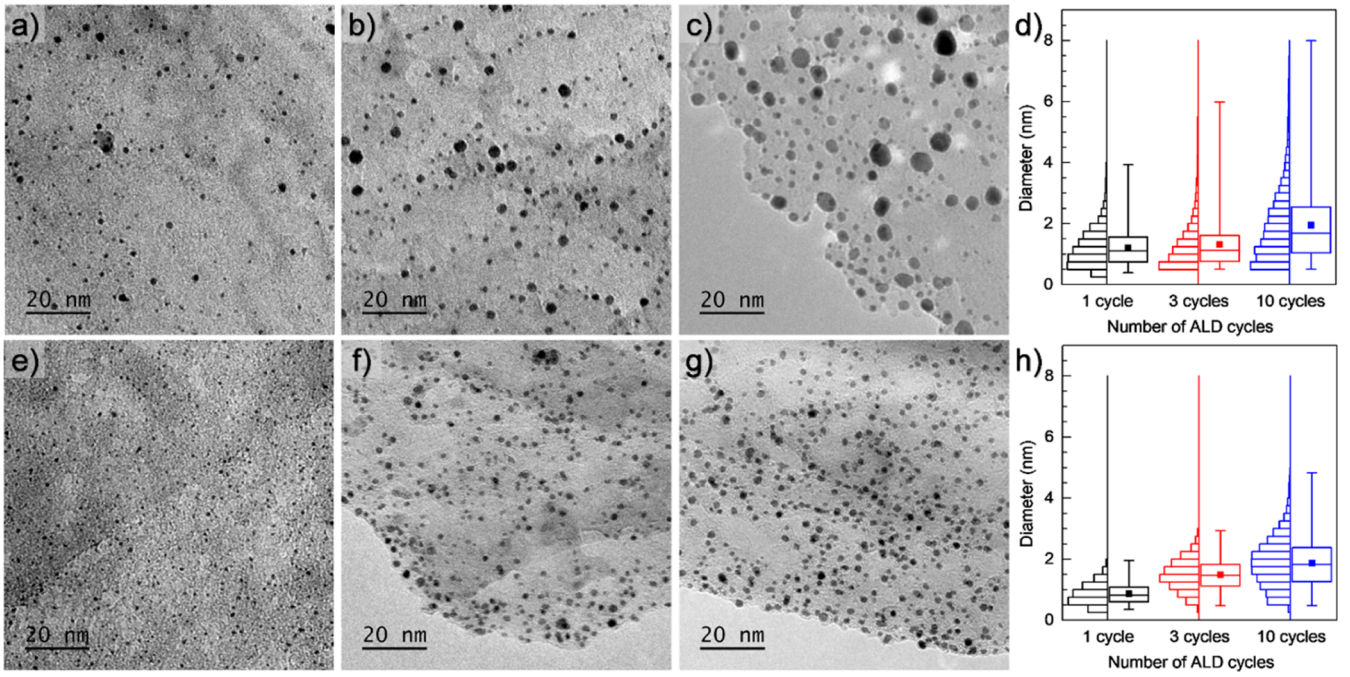

Figure 1. TEM images of the 200 °C Pt/graphene after (a) 1 cycle, (b) 3 cycles, (c) 10 cycles, and (d) their number-based PSDs; TEM images of the 200 °C/R_T Pt/graphene after (e) 1 cycle, (f) 3 cycles, (g) 10 cycles, and (h) their number-based PSDs. Each PSD includes a whisker-box plot (right) and the corresponding data overlap with a bin size of 0.25 nm (left). The boxes indicate the 25th and 90th percentiles of the population, the whiskers cover from the minimum to the maximum sizes, and the squares (■) indicate the mean diameters.

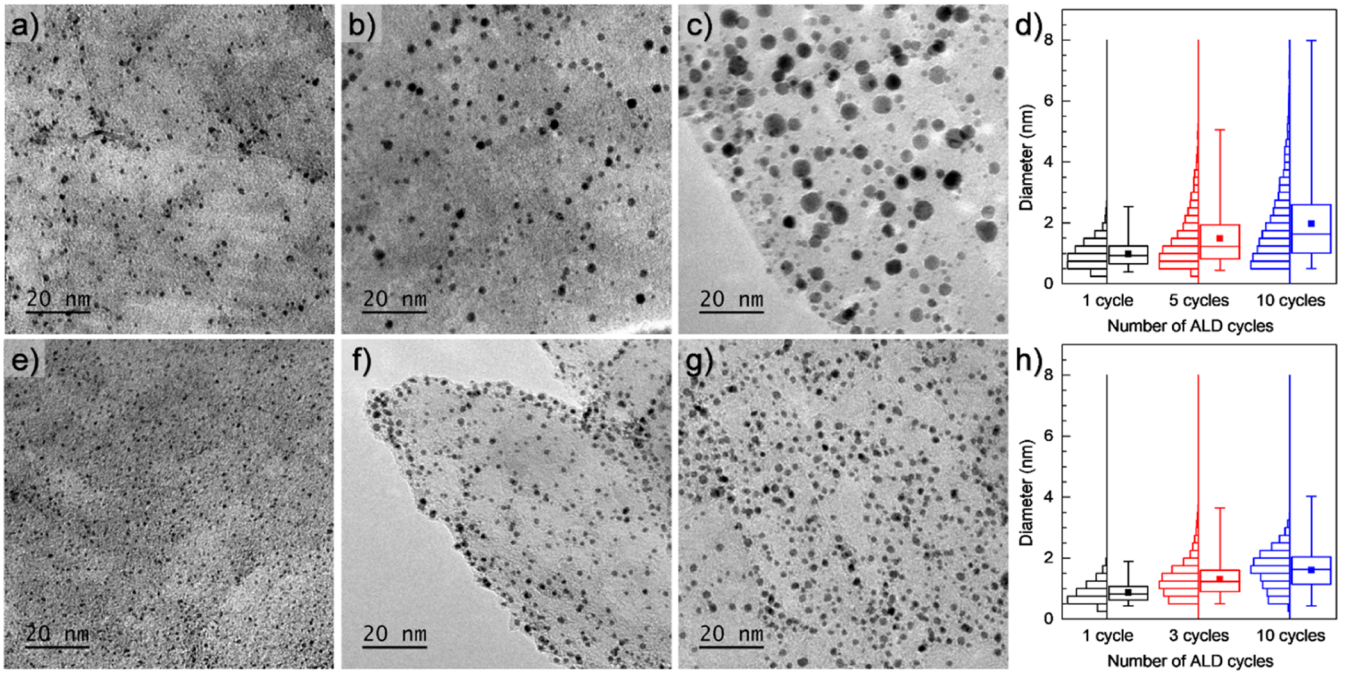

Figure 2. TEM images of the 150 °C Pt/graphene after 1 cycle (a), 3 cycles (b), 10 cycles (c), and their number-based PSDs (d); TEM images of the 150 °C/R_T Pt/graphene after 1 cycle (e), 3 cycles (f), 10 cycles (g), and their number-based PSDs (h). The PSDs are presented in the whisker-box plots with data overlap as explained in the caption of Figure 1.

temperature controller. The analysis section, which was connected to the outlet of the reactor, was used to monitor the concentration of propene, CO_2, and H_2O. This section consisted of a gas chromatograph Chrompack CP 9001, a thermal conductivity detector (TCD), and a flame ionization detector (FID). The entire setup was controlled by LabVIEW programming. Each test consisted of two heating and cooling cycles between room temperature and 450 °C with a ramp rate of 2 °C min^{-1}, followed by two tests at constant reaction temperatures of 220 and 200 °C for 12 h. Prior to the catalytic test, the bed was exposed to H_2 for 5 min.

RESULTS AND DISCUSSION

Controlling Pt NPs Size by Deposition Temperature. TEM images of the Pt/graphene obtained with the conventional ALD process at 200 °C (hereafter referred to as 200 °C

https://doi.org/10.1021/acs.langmuir.5c03532
Langmuir 2025, 41, 25658−25666

Pt/graphene) after 1, 3, and 10 ALD cycles are presented in Figures 1a–c and S2–S4 (Supporting Information). The results indicate a high dispersion of Pt NPs across the graphene surface. After the first ALD cycle, the Pt NPs have a mean diameter of 1.2 nm with a standard deviation of 0.6 nm. As the number of cycles increases to 3 and 10, the mean diameter of the NPs increases to 1.3 and 2.0 nm with standard deviations of 0.8 and 1.4 nm, respectively. The significant increase in standard deviation indicates greater nonuniformity in particle size for the higher number of cycles. In addition, the PSDs in Figure 1d show a persistent peak around 1 nm, which is attributed to the continuous formation of new nuclei in every ALD cycle. The PSDs also indicate a broad right-skewed tail as the number of ALD cycles increases, which arises from the diffusion and coalescence of existing particles.[35] This coalescence results in the formation of a considerable amount (>1%) of large Pt NPs with diameters in the range of 6–8 nm. The simultaneous new nuclei formation and the particle coalescence reduce the ability of controlling the particle size in ALD at high temperatures.

In contrast, the temperature-variation ALD process, in which the $MeCpPtMe_3$ exposure is carried out at 200 °C and the O_2 exposure is at room temperature (hereafter referred to as 200 °C/R_T Pt/graphene), produces smaller and more uniform Pt NPs for the same number of ALD cycles, as indicated by Figures 1e–g and S5–S7 (Supporting Information). Particularly, the mean diameters of the Pt NPs are 0.9, 1.5, and 1.9 nm after 1, 3, and 10 cycles, respectively, which are comparable to those of the conventional process at 200 °C. However, the standard deviations are significantly smaller, i.e., 0.3, 0.5, and 0.8 nm, indicating improved size uniformity. The absence of large-sized particles in the TEM images suggests that the temperature-variation process effectively hinders the coalescence. Consequently, virtually no Pt NPs larger than 4 nm are found, as indicated by the whiskers in Figure 1h. Moreover, the PSDs in Figure 1h gradually shift toward the right side as the number of ALD cycles increases, but remain narrow, indicating that the formation of new particles is significantly reduced, and the deposition primarily occurs on pre-existing Pt NPs.

Similar trends are observed in the ALD processes at 150 °C (Figure 2). The conventional ALD results in well-dispersed Pt NPs (Figures 2a–c and S8–S10, Supporting Information), with a gradual increase in particle size as the number of ALD cycles increases. The PSDs in Figure 2d show broader profiles analogous to those observed at 200 °C. In contrast, the temperature-variation ALD process at 150 °C/R_T (Figures 2e–g and S11–S13, Supporting Information) results in much smaller and more uniform Pt NPs, indicated by the significantly narrower PSDs in Figure 2h. The results demonstrate that both the temperature-variation ALD processes, 200 °C/R_T and 150 °C/R_T, effectively reduce the NP coalescence and new nuclei formation, thereby providing superior control over Pt NPs size and distribution compared to the conventional ALD processes. We note that the sintering of Pt NPs due to diffusion and coalescence during the conventional ALD process can be reduced by lowering the deposition temperature (i.e., to 100 °C), which leads to a narrower PSD and improved size uniformity compared to processes conducted at 150 and 200 °C.[39] However, when applying the temperature-variation ALD at this temperature, i.e., the $MeCpPtMe_3$ exposure at 100 °C followed by the oxidation step at room temperature, the PSD becomes even narrower (Figure S14). This further demonstrates the effectiveness of the temperature-variation strategy in achieving controlled NP size distribution and uniformity.

It is important to note that the deposition of Pt in ALD using $MeCpPtMe_3$ and O_2 typically requires elevated temperatures; however, in this work, crystalline Pt NPs were obtained even when the oxidation step was carried out at room temperature. This decrease in the oxidation temperature can be attributed to the use of a high O_2 partial pressure (200 mbar) combined with prolonged exposure times (600 s), in contrast to conventional ALD conditions that employ only a few mbar and a few seconds of O_2 exposure. Previous studies have shown that Pt growth does not occur at very low O_2 partial pressures (i.e., a few mTorr), even after 1000 cycles, and that nucleation delays decrease rapidly with increasing O_2 pressure.[23] More recently, it has also been demonstrated that sufficiently high O_2 exposures can enable the deposition of subnanometer Pt clusters on TiO_2 nanoparticles at room temperature.[43] These findings indicate the critical role of O_2 partial pressure in enabling Pt nucleation and determining the growth kinetics during ALD, and thus we attribute the observed decrease in the oxidation temperature primarily to the extended O_2 exposure under a high partial pressure.

It has been demonstrated earlier that the growth of Pt NPs in ALD at the temperatures of ≥150 °C is predominantly governed by the NP diffusion and coalescence rather than the single-atom processes such as precursor chemisorption, atom attachment, and Ostwald ripening.[35] In addition, it was found that the coalescence consequently promotes the new nuclei formation, and both the formation of new nuclei and the growth of pre-existing NPs have approximately the same adatom capture efficiencies.[35] Therefore, once the formation of the new nuclei is inhibited in the temperature-variation ALD process, the adsorption of the precursor molecules takes place primarily on the pre-existing Pt NPs and negligibly on bare graphene surface. This consequently reduces the amount of deposited Pt per cycle, thereby lowering the Pt loading compared to the conventional ALD process. This is indicated by the data presented in Figure 3 and Table 1. Particularly, after the first ALD cycle, all processes yield similar Pt loadings (~0.5 wt %), indicating that the adsorption of Pt precursor molecules and their subsequent reactions with O_2 proceed with comparable efficiency. However, after 3 ALD cycles, the Pt loadings achieved for the temperature-variation processes are

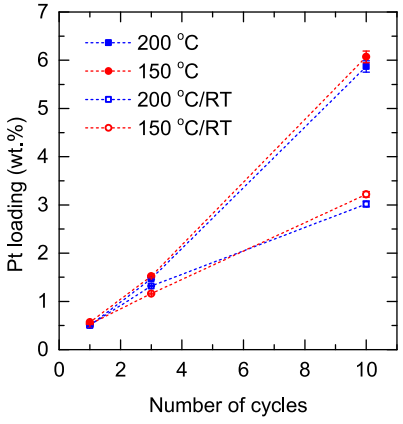

Figure 3. Pt loading as a function of the number of ALD cycles obtained with the conventional and the temperature-variation ALD processes.

https://doi.org/10.1021/acs.langmuir.5c03532
Langmuir 2025, 41, 25658–25666

Table 1. Mean Diameter, Standard Deviation and Pt Loading of Pt NPs Deposited Obtained with Different ALD Processes After 1, 3, and 10 Cycles

	catalysts											
parameters	200 °C Pt/graphene			200 °C/R_T Pt/graphene			150 °C Pt/graphene			150 °C/R_T Pt/graphene		
number of cycles	1	3	10	1	3	10	1	3	10	1	3	10
mean diameter [nm]	1.2	1.3	2	0.9	1.5	1.9	1.0	1.5	2.0	0.9	1.3	1.6
standard deviation [nm]	0.6	0.8	1.4	0.3	0.5	0.8	0.4	0.9	1.4	0.3	0.6	0.6
Pt loading [wt %]	0.5	1.5	5.9	0.5	1.3	3.0	0.6	1.5	6.1	0.5	1.2	3.2

slightly lower than those obtained with the conventional process. After 10 cycles, the Pt loading for the temperature-variation process is approximately half that of the conventional process. The results suggest that the two ALD modes follow two distinct growth mechanisms. In the conventional ALD, new nuclei continue to form alongside the growth of existing NPs, resulting in higher Pt precursor capture. In contrast, the temperature-variation ALD effectively suppresses the nucleation of new particles, limiting the number of adsorption sites available for the precursor in subsequent cycles. Consequently, precursor molecules are predominantly consumed for the growth of pre-existing NPs, leading to a reduced Pt loading but a narrower PSD and more uniform particle sizes.

HR-TEM images of the 200 °C Pt/graphene and the 200 °C/R_T Pt/graphene after 10 cycles reveal a high degree of crystallinity in the Pt NPs (Figures 4a,b and S15−S18). The measurements on selected Pt NPs show the lattice spacing values of 0.236 and 0.138 nm, corresponding to the interplanar spacings of the (111) and (220) families of the face-centered cubic (FCC) structure of Pt.[44] This is consistent with the XRD diffractograms presented in Figure 4c. Aside from the peaks attributed to the graphene substrate, the XRD diffractograms of both the 200 and 150 °C Pt/graphene catalysts exhibit distinct peaks at 40.03°, 46.44°, 67.83°, and 81.62°, which correspond to the (111), (200), (220), and (311) planes of the Pt FCC structure. However, the diffractograms of the catalysts obtained with the room-temperature step (200 °C/R_T and 150 °C/R_T) show a dominant (111) peak, with significantly reduced intensities for the other planes. This suggests a preferred orientation along the (111) plane, as indicated by the HR-TEM images (Figures 4b and S16−S18).

The XPS spectra of the Pt/graphene obtained by the temperature-variation ALD are shown in Figure 4d,e. The survey scans indicate the presence of the Pt peaks, including Pt 4p, Pt 4d and Pt 4f, as denoted in the figure. The high-resolution Pt 4f XPS spectra in Figure 4e reveal two distinct peaks, Pt $4f_{7/2}$ and Pt $4f_{5/2}$, which arise from the splitting of the 4f core-level states caused by the interaction between the spin and orbital angular momentum of the electrons.[45] For metallic Pt NPs, the Pt $4f_{7/2}$ peak typically appears at a binding energy between 70.9 and 71.3 eV, with the Pt $4f_{5/2}$ peak located approximately 3.3 eV higher.[46,47] In contrast, for oxidized Pt (e.g., Pt^{2+} or Pt^{4+}), the Pt 4f peaks shift to higher binding energies. Specifically, the Pt $4f_{7/2}$ peak for Pt^{2+} (e.g., PtO) shifts above 72.0 eV, while for Pt^{4+} (e.g., PtO_2), it shifts further above 74.0 eV.[48] In this study, the main Pt $4f_{7/2}$ peak is centered around 71.2 eV, while the Pt $4f_{5/2}$ peak is positioned around 74.5 eV. These binding energies are consistent with metallic Pt (Pt^0). Additionally, all spectra display sharp and symmetrical peaks, indicating that the Pt NPs are in the metallic state. Notably, the relative intensity and binding energy positions of the peaks remain unchanged for all deposition conditions, suggesting that Pt maintains its metallic state regardless of the ALD process temperature.

Catalytic Performance and Stability of Pt/Graphene Catalysts. Figure 5 presents the catalytic performance of the 200 °C/R_T Pt/graphene in propene oxidation reactions. The catalyst was subjected to two thermal cycles, involving heating and cooling between room temperature and 450 °C (Figure 5a), followed by two consecutive 12 h tests at 200 and 220 °C (Figure 5b,c). The temperature-programmed oxidation (TPO) curves in Figure 5a show a complete propene conversion for the catalyst. For comparison, the catalytic performance of the 200 °C Pt/graphene under the same experimental conditions, which was reported in the previous study,[39] was added (the dotted plots). Notably, the 200 °C/R_T Pt/graphene achieves 100% conversion at a slightly lower temperature (∼220 °C) compared to the 200 °C Pt/graphene (∼230 °C), indicating its higher catalytic activity. Importantly, the Pt loading of the 200 °C/R_T Pt/graphene is approximately half that of the 200 °C Pt/graphene, as presented in Table 1. This emphasizes the enhanced catalytic efficiency of the 200 °C/R_T Pt/graphene and demonstrates that the temperature-variation ALD process can deliver catalysts with superior performance at a reduced Pt content.

The results presented in Figure 5b,c further highlight the superior performance of the 200 °C/R_T Pt/graphene. At 200 °C, the propene conversion obtained with the 200 °C/R_T is ∼46%, compared to ∼30% for the 200 °C Pt/graphene. At 220 °C, the 200 °C/R_T Pt/graphene achieves a full conversion (100%), while the 200 °C Pt/graphene reaches ∼65%. Both catalysts exhibit stable catalytic activity after the performance and stability tests. However, the TEM images in Figures 5d,e and S19−S20 reveal a greater degree of Pt NP coalescence for the 200 °C Pt/graphene, leading to a broader PSD, as indicated in Figure 5f. The average Pt NP size in the 200 °C Pt/graphene increases to 4.2 nm with a standard deviation of 4.1 nm, compared to 2.7 and 1.0 nm, respectively, for the 200 °C/R_T Pt/graphene. The observed difference in the sintering behavior between the Pt NPs produced by the conventional ALD and those obtained via the temperature-variation ALD can be attributed to their distinct PSDs and uniformity. In the conventional ALD case, the broad PSD and nonuniform NP sizes create a strong driving force for Ostwald ripening and coalescence, as smaller particles tend to dissolve and redeposit onto larger ones, accelerating sintering.[49,50] In contrast, the temperature-variation ALD produces a narrow PSD with more uniform NP sizes, which minimizes the size-dependent chemical potential differences between particles and thereby suppresses Ostwald ripening. The results emphasize the critical importance of achieving uniform particle size for optimal catalytic performance and durability, thereby indicating the potential of the temperature-variation ALD approach in synthesizing high-performance Pt catalysts.

https://doi.org/10.1021/acs.langmuir.5c03532
Langmuir 2025, 41, 25658−25666

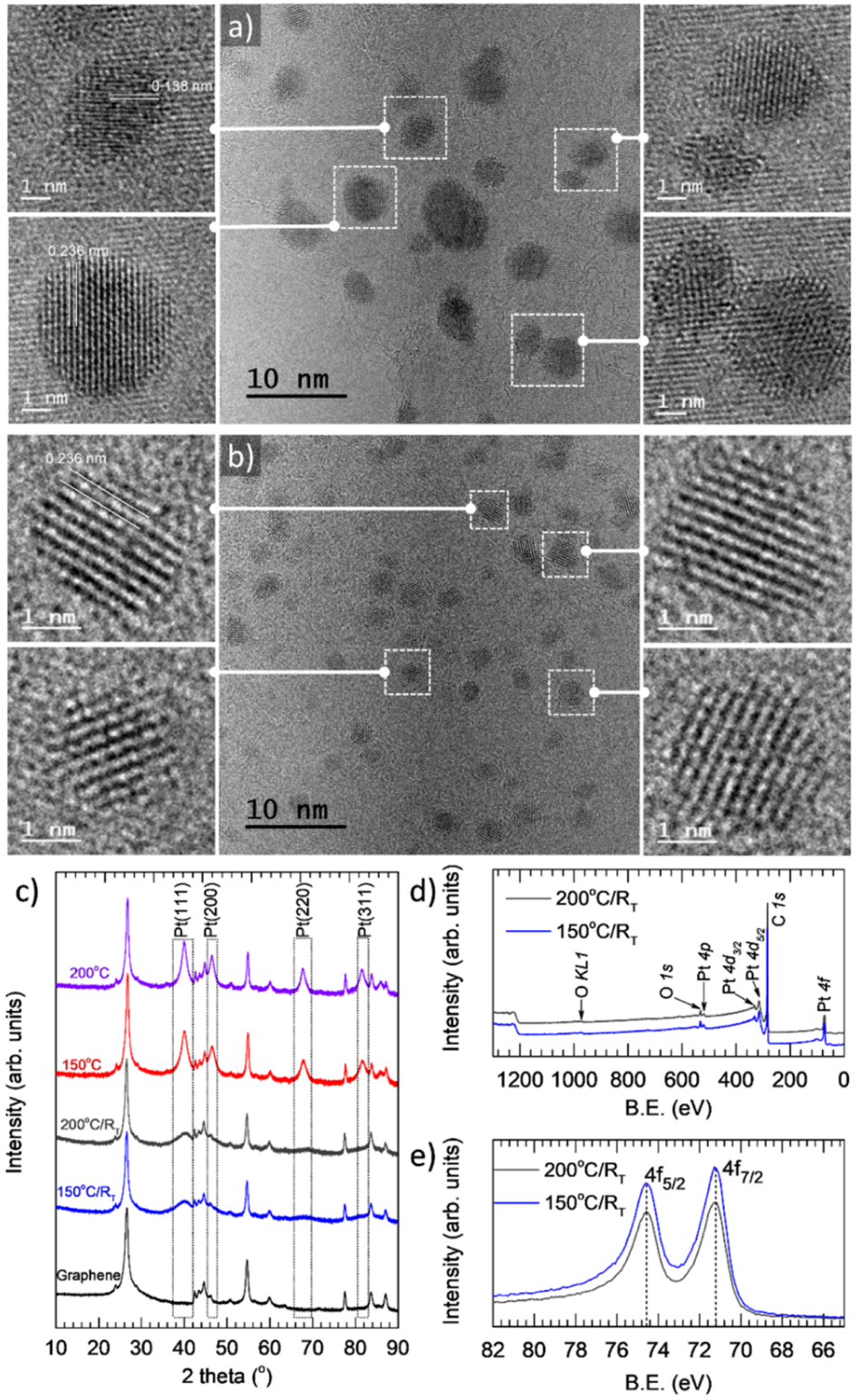

Figure 4. HR-TEM images of (a) the 200 °C Pt/graphene, (b) the 200 °C/R_T Pt/graphene after 10 ALD cycles. The satellite images are HR-TEM images of selected particles in (a,b); (c) XRD diffractograms of the initial graphene and the Pt/graphene obtained with different processes; XPS spectra of the 150 °C/R_T and 200 °C/R_T Pt/graphene after 10 ALD cycles: (d) survey scan and (e) Pt 4f core-level spectra.

CONCLUSIONS

In summary, this work presents a new strategy to control the growth of Pt NPs on graphene in ALD using $MeCpPtMe_3$ and O_2. By lowering the temperature during the O_2 exposure to room temperature, the diffusion and coalescence of Pt NPs can be effectively suppressed. This reduces the new nuclei formation and the mobility of deposited NPs, promoting the deposition on pre-existing Pt NPs, resulting in highly dispersed Pt NPs with narrow PSDs. The comprehensive material characterizations with HR-TEM, XRD and XPS confirmed the high crystallinity and metallic state of the Pt NPs deposited by

https://doi.org/10.1021/acs.langmuir.5c03532
Langmuir 2025, 41, 25658−25666

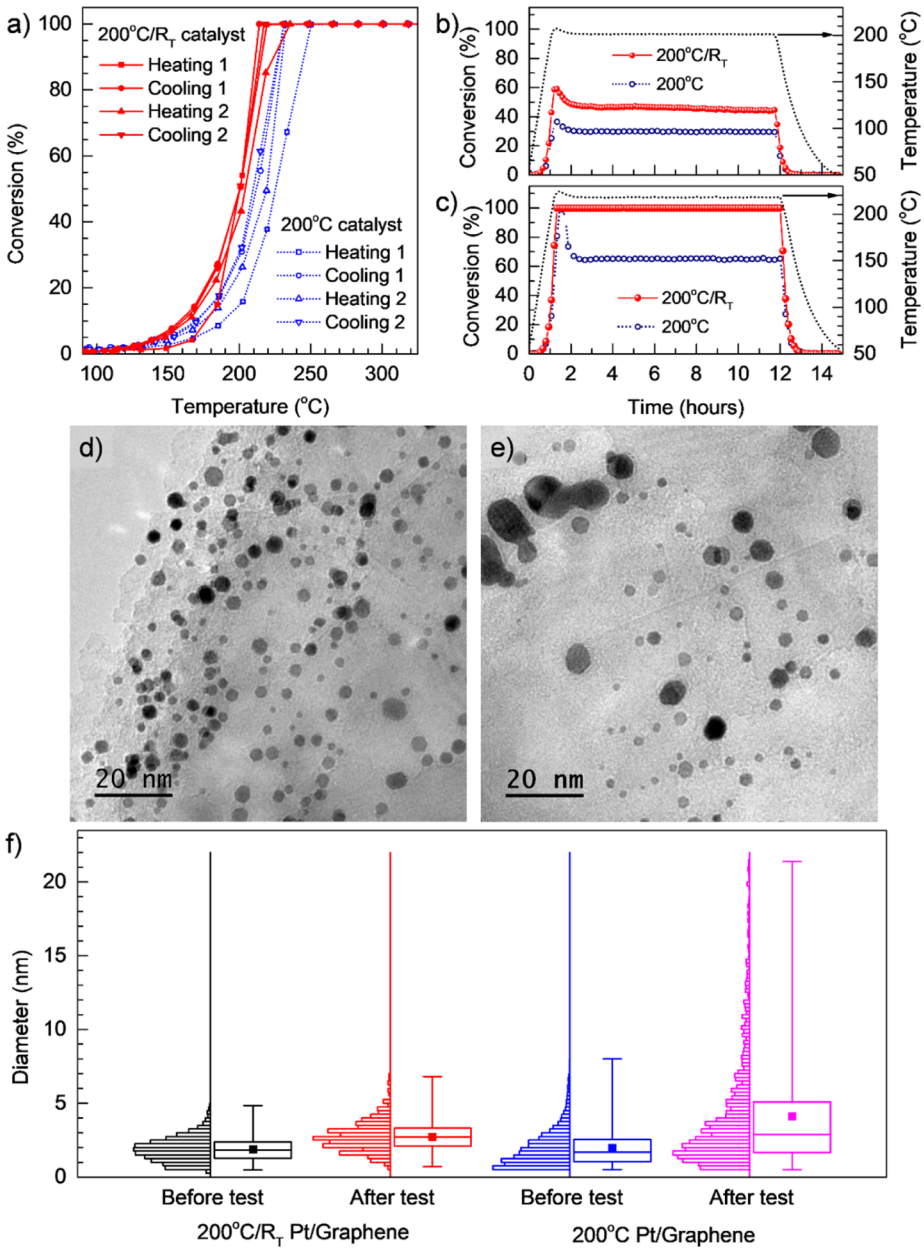

Figure 5. Catalytic performance of the 200 °C/R_T Pt/graphene catalyst under different conditions: (a) heating and cooling cycles between room temperature and 450 °C, constant reaction temperatures of (b) 200 °C and (c) 220 °C for 12 h. For comparison, the catalytic performances of the 200 °C Pt/graphene catalyst under the same conditions are added. TEM images of (d) the 200 °C/R_T Pt/graphene and (e) the 200 °C Pt/graphene catalysts after the catalytic tests; (f) PSDs of the catalysts before and after the tests.

the temperature-variation process. The Pt/graphene catalyst with a narrower particle size distribution exhibits higher catalytic activity and stability against coalescence despite its significantly lower Pt loading, which is demonstrated by the propene oxidation reaction. The results indicate the potential of the temperature-variation ALD to deliver efficient, high-performance Pt-based catalysts with reduced Pt usage, paving the way for more sustainable use of noble metals.

■ ASSOCIATED CONTENT

Supporting Information

The Supporting Information is available free of charge at https://pubs.acs.org/doi/10.1021/acs.langmuir.5c03532.

Schematic drawing of the FBR-ALD system (Figure S1); TEM images taken at different areas with different magnifications of the 200 °C Pt/graphene after 1, 3, and 10 cycles (Figures S2, S3 and S4, respectively); TEM images taken at different areas with different magnifications of the 200 °C/R_T Pt/graphene after 1, 3, and 10 cycles (Figures S5, S6 and S7, respectively); TEM images taken at different areas with different magnifications of the 150 °C Pt/graphene after 1, 3, and 10 cycles (Figures S8, S9 and S10, respectively); TEM images taken at different areas with different magnifications of the 150 °C/R_T Pt/graphene after 1, 3, and 10 cycles (Figures S11, S12 and S13, respectively); TEM images and PSDs of the 100 °C/100 °C Pt/graphene and 100 °C/R_T Pt/graphene after 10 cycles (Figure S14); HR-TEM images taken at different areas with different magnifications of the 200 °C Pt/graphene and the 200

https://doi.org/10.1021/acs.langmuir.5c03532
Langmuir 2025, 41, 25658−25666

°C Pt/graphene after 10 cycles (Figures S15−S18). TEM images of the 200 °C/R_T Pt/graphene and 200 °C Pt/graphene (10 cycles) after the catalytic test (Figures S19 and S20, respectively) (PDF)

AUTHOR INFORMATION

Corresponding Author

Hao Van Bui − *Faculty of Materials Science and Engineering, Phenikaa University, Hanoi 12116, Vietnam;* orcid.org/0000-0001-8460-1409; Email: hao.buivan@phenikaa-uni.edu.vn

Authors

Sri Sharath Kulkarni − *Product & Process Engineering, Department of Chemical Engineering, Faculty of Applied Sciences, Delft University of Technology, 2629 HZ Delft, The Netherlands*

J. Ruud van Ommen − *Product & Process Engineering, Department of Chemical Engineering, Faculty of Applied Sciences, Delft University of Technology, 2629 HZ Delft, The Netherlands;* orcid.org/0000-0001-7884-0323

Complete contact information is available at: https://pubs.acs.org/10.1021/acs.langmuir.5c03532

Notes

The authors declare no competing financial interest.

ACKNOWLEDGMENTS

The authors acknowledge Dr. Meng Yue Yang (National Centre for High-Resolution Electron Microscopy, TU Delft) for the HR-TEM imaging and Baukje Terpstra (Reactor Institute Delft) for INAA analysis. H.V.B. acknowledges the funding from Phenikaa Innovation Foundation (Phenikaa Group), under the grant number ĐMST.2022.03.

REFERENCES

(1) Hansen, J. N.; Prats, H.; Toudahl, K. K.; Mørch Secher, N.; Chan, K.; Kibsgaard, J.; Chorkendorff, I. Is There Anything Better than Pt for HER? *ACS Energy Lett.* **2021**, *6* (4), 1175−1180.

(2) Huang, L.; Zaman, S.; Tian, X.; Wang, Z.; Fang, W.; Xia, B. Y. Advanced Platinum-Based Oxygen Reduction Electrocatalysts for Fuel Cells. *Acc. Chem. Res.* **2021**, *54* (2), 311−322.

(3) Qiao, Z.; Wang, C.; Zeng, Y.; Spendelow, J. S.; Wu, G. Advanced Nanocarbons for Enhanced Performance and Durability of Platinum Catalysts in Proton Exchange Membrane Fuel Cells. *Small* **2021**, *17* (48), 2006805.

(4) Li, J.; Guan, Q.; Wu, H.; Liu, W.; Lin, Y.; Sun, Z.; Ye, X.; Zheng, X.; Pan, H.; Zhu, J.; Chen, S.; Zhang, W.; Wei, S.; Lu, J. Highly Active and Stable Metal Single-Atom Catalysts Achieved by Strong Electronic Metal−Support Interactions. *J. Am. Chem. Soc.* **2019**, *141* (37), 14515−14519.

(5) Han, B.; Guo, Y.; Huang, Y.; Xi, W.; Xu, J.; Luo, J.; Qi, H.; Ren, Y.; Liu, X.; Qiao, B.; Zhang, T. Strong Metal−Support Interactions between Pt Single Atoms and TiO_2. *Angew. Chem., Int. Ed.* **2020**, *59* (29), 11824−11829.

(6) Ma, L.; Wang, C.; Xia, B. Y.; Mao, K.; He, J.; Wu, X.; Xiong, Y.; Lou, X. W. (David). Platinum Multicubes Prepared by Ni2+-Mediated Shape Evolution Exhibit High Electrocatalytic Activity for Oxygen Reduction. *Angew. Chem., Int. Ed.* **2015**, *54* (19), 5666−5671.

(7) Yano, H.; Watanabe, M.; Iiyama, A.; Uchida, H. Particle-Size Effect of Pt Cathode Catalysts on Durability in Fuel Cells. *Nano Energy* **2016**, *29*, 323−333.

(8) Li, C.; Clament Sagaya Selvam, N.; Fang, J. Shape-Controlled Synthesis of Platinum-Based Nanocrystals and Their Electrocatalytic Applications in Fuel Cells. *Nano-Micro Lett.* **2023**, *15* (1), 83.

(9) Huang, B.; He, Y.; Wang, Z.; Zhu, Y.; Zhang, Y.; Cen, K. High-Performance Pt Catalyst with Graphene/Carbon Black as a Hybrid Support for SO_2 Electrocatalytic Oxidation. *Langmuir* **2020**, *36* (1), 20−27.

(10) He, M.; Fei, G.; Zheng, Z.; Cheng, Z.; Wang, Z.; Xia, H. Pt Nanoparticle-Loaded Graphene Aerogel Microspheres with Excellent Methanol Electro-Oxidation Performance. *Langmuir* **2019**, *35* (10), 3694−3700.

(11) Zhou, Y.; King, D. M.; Liang, X.; Li, J.; Weimer, A. W. Optimal Preparation of Pt/TiO_2 Photocatalysts Using Atomic Layer Deposition. *Appl. Catal., B* **2010**, *101* (1), 54−60.

(12) Lee, W.-J.; Bera, S.; Kim, C. M.; Koh, E.-K.; Hong, W.-P.; Oh, S.-J.; Cho, E.; Kwon, S.-H. Synthesis of Highly Dispersed Pt Nanoparticles into Carbon Supports by Fluidized Bed Reactor Atomic Layer Deposition to Boost PEMFC Performance. *NPG Asia Mater.* **2020**, *12* (1), 1−13.

(13) Chen, Y.; Wang, Y.; Zheng, L.; Chang, Y.; Xu, S.; Wu, Y.; Zhou, W.; Lu, Y.; Wang, J.; Li, H. Platinum Nanoclusters by Atomic Layer Deposition on Three-Dimensional TiO_2 Nanotube Array for Efficient Hydrogen Evolution. *Mater. Today Energy* **2022**, *27*, 101042.

(14) Li, J.; Liang, X.; King, D. M.; Jiang, Y.-B.; Weimer, A. W. Highly Dispersed Pt Nanoparticle Catalyst Prepared by Atomic Layer Deposition. *Appl. Catal., B* **2010**, *97* (1), 220−226.

(15) Adebayo, B. O.; Yu, H.; Rownaghi, A. A.; Liang, X.; Rezaei, F. Atomic Layer Deposited Pt/TiO_2-SiO_2 and Pt/ZrO_2-SiO_2 for Sequential Adsorption and Oxidation of VOCs. *Chem. Eng. J.* **2022**, *444*, 136603.

(16) Lee, W.-J.; Bera, S.; Woo, H.-J.; Hong, W.; Park, J.-Y.; Oh, S.-J.; Kwon, S.-H. Atomic Layer Deposition Enabled PtNi Alloy Catalysts for Accelerated Fuel-Cell Oxygen Reduction Activity and Stability. *Chem. Eng. J.* **2022**, *442*, 136123.

(17) Liu, D.; Li, X.; Chen, S.; Yan, H.; Wang, C.; Wu, C.; Haleem, Y. A.; Duan, S.; Lu, J.; Ge, B.; Ajayan, P. M.; Luo, Y.; Jiang, J.; Song, L. Atomically Dispersed Platinum Supported on Curved Carbon Supports for Efficient Electrocatalytic Hydrogen Evolution. *Nat. Energy* **2019**, *4* (6), 512−518.

(18) Sun, S.; Zhang, G.; Gauquelin, N.; Chen, N.; Zhou, J.; Yang, S.; Chen, W.; Meng, X.; Geng, D.; Banis, M. N.; Li, R.; Ye, S.; Knights, S.; Botton, G. A.; Sham, T. K.; Sun, X. Single-Atom Catalysis Using Pt/Graphene Achieved through Atomic Layer Deposition. *Sci. Rep.* **2013**, *3*, 1−9.

(19) Dinh, K.-H. T.; Ta, H. T. T.; Nguyen, N. L.; Le, V. T.; Nguyen, V. H.; Van Bui, H. Dimension Control of Platinum Nanostructures by Atomic Layer Deposition: From Surface Chemical Reactions to Applications. *Chem. Mater.* **2023**, *35* (6), 2248−2280.

(20) Lu, J. Atomic Lego Catalysts Synthesized by Atomic Layer Deposition. *Acc. Mater. Res.* **2022**, *3* (3), 358−368.

(21) O'Neill, B. J.; Jackson, D. H. K.; Lee, J.; Canlas, C.; Stair, P. C.; Marshall, C. L.; Elam, J. W.; Kuech, T. F.; Dumesic, J. A.; Huber, G. W. Catalyst Design with Atomic Layer Deposition. *ACS Catal.* **2015**, *5* (3), 1804−1825.

(22) Aaltonen, T.; Ritala, M.; Sajavaara, T.; Keinonen, J.; Leskelä, M. Atomic Layer Deposition of Platinum Thin Films. *Chem. Mater.* **2003**, *15* (9), 1924−1928.

(23) MacKus, A. J. M.; Verheijen, M. A.; Leick, N.; Bol, A. A.; Kessels, W. M. M. Influence of Oxygen Exposure on the Nucleation of Platinum Atomic Layer Deposition: Consequences for Film Growth, Nanopatterning, and Nanoparticle Synthesis. *Chem. Mater.* **2013**, *25* (9), 1905−1911.

(24) Lee, H.-B.-R.; Pickrahn, K. L.; Bent, S. F. Effect of O_3 on Growth of Pt by Atomic Layer Deposition. *J. Phys. Chem. C* **2014**, *118* (23), 12325−12332.

(25) Dendooven, J.; Ramachandran, R. K.; Devloo-Casier, K.; Rampelberg, G.; Filez, M.; Poelman, H.; Marin, G. B.; Fonda, E.; Detavernier, C. Low-Temperature Atomic Layer Deposition of Platinum Using (Methylcyclopentadienyl)Trimethylplatinum and Ozone. *J. Phys. Chem. C* **2013**, *117* (40), 20557−20561.

(26) Gould, T. D.; Lubers, A. M.; Corpuz, A. R.; Weimer, A. W.; Falconer, J. L.; Medlin, J. W. Controlling Nanoscale Properties of

Supported Platinum Catalysts through Atomic Layer Deposition. *ACS Catal.* **2015**, *5* (2), 1344−1352.
(27) Lubers, A. M.; Drake, A. W.; Ludlow, D. J.; Weimer, A. W. Electrochemical Hydrogen Pumping Using a Platinum Catalyst Made in a Fluidized Bed via Atomic Layer Deposition. *Powder Technol.* **2016**, *296*, 72−78.
(28) Lubers, A. M.; Muhich, C. L.; Anderson, K. M.; Weimer, A. W. Mechanistic Studies for Depositing Highly Dispersed Pt Nanoparticles on Carbon by Use of Trimethyl(Methylcyclopentadienyl)-Platinum(IV) Reactions with O_2 and H_2. *J. Nanopart. Res.* **2015**, *17* (4), 179.
(29) Aaltonen, T.; Rahtu, A.; Ritala, M.; Leskelä, M. Reaction Mechanism Studies on Atomic Layer Deposition of Ruthenium and Platinum. *Electrochem. Solid-State Lett.* **2003**, *6* (9), C130.
(30) Kessels, W. M. M.; Knoops, H. C. M.; Dielissen, S. A. F.; MacKus, A. J. M.; Van De Sanden, M. C. M. Surface Reactions during Atomic Layer Deposition of Pt Derived from Gas Phase Infrared Spectroscopy. *Appl. Phys. Lett.* **2009**, *95* (1), 1−4.
(31) Liang, X.; Zhou, Y.; Li, J.; Weimer, A. W. Reaction Mechanism Studies for Platinum Nanoparticle Growth by Atomic Layer Deposition. *J. Nanopart. Res.* **2011**, *13* (9), 3781−3788.
(32) Vandalon, V.; Mackus, A. J. M.; Kessels, W. M. M. Surface Chemistry during Atomic Layer Deposition of Pt Studied with Vibrational Sum-Frequency Generation. *J. Phys. Chem. C* **2022**, *126* (5), 2463−2474.
(33) Mackus, A. J. M.; Leick, N.; Baker, L.; Kessels, W. M. M. Catalytic Combustion and Dehydrogenation Reactions during Atomic Layer Deposition of Platinum. *Chem. Mater.* **2012**, *24* (10), 1752−1761.
(34) Grillo, F.; Van Bui, H.; La Zara, D.; Aarnink, A. A. I.; Kovalgin, A. Y.; Kooyman, P.; Kreutzer, M. T.; van Ommen, J. R. From Single Atoms to Nanoparticles: Autocatalysis and Metal Aggregation in Atomic Layer Deposition of Pt on TiO_2 Nanopowder. *Small* **2018**, *14* (23), 1800765.
(35) Grillo, F.; Van Bui, H.; Moulijn, J. A.; Kreutzer, M. T.; Van Ommen, J. R. Understanding and Controlling the Aggregative Growth of Platinum Nanoparticles in Atomic Layer Deposition: An Avenue to Size Selection. *J. Phys. Chem. Lett.* **2017**, *8* (5), 975−983.
(36) Van Bui, H.; Grillo, F.; Van Ommen, J. R. Atomic and Molecular Layer Deposition: Off the Beaten Track. *Chem. Commun.* **2017**, *53* (1), 45−71.
(37) George, S. M. Atomic Layer Deposition: An Overview. *Chem. Rev.* **2010**, *110* (1), 111−131.
(38) Goulas, A.; Ruud van Ommen, J. Atomic Layer Deposition of Platinum Clusters on Titania Nanoparticles at Atmospheric Pressure. *J. Mater. Chem. A* **2013**, *1* (15), 4647−4650.
(39) Van Bui, H.; Grillo, F.; Kulkarni, S. S.; Bevaart, R.; Van Thang, N.; van der Linden, B.; Moulijn, J. A.; Makkee, M.; Kreutzer, M. T.; van Ommen, J. R. Low-Temperature Atomic Layer Deposition Delivers More Active and Stable Pt-Based Catalysts. *Nanoscale* **2017**, *9* (30), 10802−10810.
(40) Chu, Y. F.; Ruckenstein, E. Behavior of Platinum Crystallites on Carbon Substrates. *Surf. Sci.* **1977**, *67* (2), 517−540.
(41) Beetstra, R.; Lafont, U.; Nijenhuis, J.; Kelder, E. M.; van Ommen, J. R. Atmospheric Pressure Process for Coating Particles Using Atomic Layer Deposition. *Chem. Vap. Deposition* **2009**, *15* (7−9), 227−233.
(42) Sartipi, S.; Jansma, H.; Bosma, D.; Boshuizen, B.; Makkee, M.; Gascon, J.; Kapteijn, F. Six-Flow Operations for Catalyst Development in Fischer−Tropsch Synthesis: Bridging the Gap between High-Throughput Experimentation and Extensive Product Evaluation. *Rev. Sci. Instrum.* **2013**, *84* (12), 124101.
(43) Van Bui, H.; Nguyen, A. P.; Dang, M. D.; Dinh, T. D.; Kooyman, P. J.; Ruud Van Ommen, J. What Could Be the Low-Temperature Limit of Atomic Layer Deposition of Platinum Using $MeCpPtMe_3$ and Oxygen? *Chem. Commun.* **2024**, *60* (95), 14045−14048.
(44) Miyazawa, K.; Yoshitake, M.; Tanaka, Y. HRTEM Analyses of the Platinum Nanoparticles Prepared on Graphite Particles Using Coaxial Arc Plasma Deposition. *J. Nanopart. Res.* **2017**, *19* (6), 191.
(45) Major, G. H.; Fairley, N.; Sherwood, P. M. A.; Linford, M. R.; Terry, J.; Fernandez, V.; Artyushkova, K. Practical Guide for Curve Fitting in X-Ray Photoelectron Spectroscopy. *J. Vac. Sci. Technol., A* **2020**, *38* (6), 061203.
(46) Contour, J. P.; Mouvier, G.; Hoogewys, M.; Leclere, C. X-Ray Photoelectron Spectroscopy and Electron Microscopy of Pt-Rh Gauzes Used for Catalytic Oxidation of Ammonia. *J. Catal.* **1977**, *48* (1), 217−228.
(47) Aricò, A. S.; Shukla, A. K.; Kim, H.; Park, S.; Min, M.; Antonucci, V. An XPS Study on Oxidation States of Pt and Its Alloys with Co and Cr and Its Relevance to Electroreduction of Oxygen. *Appl. Surf. Sci.* **2001**, *172* (1), 33−40.
(48) Bancroft, G. M.; Adams, I.; Coatsworth, L. L.; Bennewitz, C. D.; Brown, J. D.; Westwood, W. D. ESCA Study of Sputtered Platinum Films. *Anal. Chem.* **1975**, *47* (3), 586−588.
(49) Molleman, B.; Hiemstra, T. Size and Shape Dependency of the Surface Energy of Metallic Nanoparticles: Unifying the Atomic and Thermodynamic Approaches. *Phys. Chem. Chem. Phys.* **2018**, *20* (31), 20575−20587.
(50) Yao, Y.; Wei, Y.; Chen, S. Size Effect of the Surface Energy Density of Nanoparticles. *Surf. Sci.* **2015**, *636*, 19−24.

https://doi.org/10.1021/acs.langmuir.5c03532
Langmuir 2025, 41, 25658−25666